Available online at www.sciencedirect.com
SCIENCE DIRECT®
Journal of Power Sources 122 (2003) 188–194
JOURNAL OF POWER SOURCES
www.elsevier.com/locate/jpowsour

# Characterization of high-power lithium-ion cells during constant current cycling
## Part I. Cycle performance and electrochemical diagnostics

Joongpyo Shim, Kathryn A. Striebel*

*Lawrence Berkeley National Laboratory, Environmental Energy Technologies Division, Berkeley, CA 94720, USA*

Received 29 January 2003; accepted 13 February 2003

**Abstract**

Twelve $cm^2$ pouch type lithium-ion cells were assembled with graphite anodes, $LiNi_{0.8}Co_{0.15}Al_{0.05}O_2$ cathodes and 1 M $LiPF_6$/EC/DEC electrolyte. These pouch cells were cycled at different depths of discharge (100 and 70% DOD) at room temperature to investigate cycle performance and pulse power capability. The capacity loss and power fade of the cells cycled over 100% DOD was significantly faster than the cell cycled over 70% DOD. The overall cell impedance increased with cycling, although the ohmic resistance from the electrolyte was almost constant. From electrochemical analysis of each electrode after cycling, structural and/or impedance changes in the cathode are responsible for most of the capacity and power fade, not the consumption of cycleable Li from side-reactions.


*Keywords:* Lithium-ion battery; Cycle performance; Capacity fade; Impedance

## 1. Introduction

Lithium-ion batteries have been intensively studied for application in all-electric and hybrid electric vehicles (HEVs) because of their high-power and energy densities [1–3]. The Generation 2 cell chemistry, proposed by the Advanced Technology Development (ATD) program is considered to be a good candidate for the hybrid electric vehicle. This chemistry includes doped lithium nickel oxide ($LiNiO_2$) as the active cathode material and synthetic graphite as the anode [4]. The focus of the ATD program is the characterization of the performance of high-power lithium-ion cells during calendar life and pulse power cycling with the power profiles developed by PNGV [5,6] and to determine capacity and power fade mechanisms through advanced diagnostics [7]. In support of this effort, the parallel program, Batteries for Advanced Transportation Technologies (BATT) is studying this cell chemistry under constant current cycling regimes with standard test protocols and diagnostic techniques to determine cycle performance and capacity fade mechanisms [8,9].

Lithium nickel oxide is a promising cathode material in the lithium-ion battery because of lower cost and higher initial capacity compared to $LiCoO_2$. However, the problem of $LiNiO_2$ is the serious phase transition from hexagonal through monoclinic to other hexagonal during lithium intercalation/deintercalation between 3.0 and 4.3 V. The partial substitution of Ni with Co can stabilize the lithium nickel oxide structure on cycling, especially at the higher voltages [10,11]. The addition of Al limits the possibility of over-charge even further and improves the thermal stability and safety aspects of the oxide [12,13].

In a previous study with $LiNi_{0.8}Co_{0.15}Al_{0.05}O_2$/graphite pouch cells, capacity fade during constant current cycling at elevated temperature was examined [8]. Studies included cycling cells at different temperatures, followed by electrochemical, physical and spectroscopic diagnostics on the cell components removed from the cycled cells. During 100% depth of discharge (DOD) cycling at 60 °C, the performance of the cathode was severely reduced by a loss of electronic conductivity. In addition, the anode was found to contain a large amount of $Li_2CO_3$, although its performance compared quite well with that of a fresh anode. In this work, the performance of lab-size $LiNi_{0.8}Co_{0.15}Al_{0.05}O_2$/graphite pouch cells during extended (1000 cycles) room temperature cycling over different capacity ranges was examined. The capacity fade, as well as pulse power capability and impedance changes, were monitored during different depth of discharge cycling. As before, the cell components were

* Corresponding author. Tel.: +1-510-486-4385; fax: +1-510-486-7303.
*E-mail address:* kastriebel@lbl.gov (K.A. Striebel).

0378-7753/03/$ – see front matter © 2003 Elsevier Science B.V. All rights reserved.
doi:10.1016/S0378-7753(03)00351-3

examined with electrochemical diagnostics to help to define the performance fade mechanisms. Chemical and physical diagnostic analyses of the cell components are the subject of Part II [14].

## 2. Experimental

The positive electrode and negative electrodes were used as received from Quallion Corp. and comprised $LiNi_{0.8}Co_{0.15}Al_{0.05}O_2$ (Fuji Chemical) coated on aluminum foil current collector and graphite (MAG-10, Hitachi Chemical) coated on copper foil. The electrode details are listed in Table 1. The electrolyte was 1 M $LiPF_6$ in 1:1 ethylene carbonate (EC)/diethyl carbonate (DEC) (LP40, EM Science). The pouch cells were assembled in an Ar-filled glove box. The separator was Celgard 2500 with a thickness of 25 μm to reserve the electrolyte and prevent contact between positive and negative electrodes. The copper and aluminum current collectors were welded to nickel and aluminum tabs with an ultrasonic welder. Active areas of both electrodes were 12 $cm^2$ (3 cm × 4 cm).

After assembly, the cells were charged and discharged for two cycles at a very slow rate (*C*/25) with a Maccor Battery Cycler for the formation of a smooth SEI layer on the surface of the anode. After formation, the pouch cells were charged to 4.1 V at constant current (*C*/2) and then held at 4.1 V until the current dropped below *C*/20 or for a maximum of 2 h. After a rest period of 15 min, cells were discharged to 3.0 V at constant current (*C*/2) to either 100 or 70% DOD. Cycling was interrupted after every 80 cycles to measure cell impedance and pulse power capability with the hybrid pulse power characterization (HPPC) profile. The HPPC profile was designed to measure dynamic power capability during both discharge and charge pulses [5]. As shown in Fig. 1, the HPPC test consists of repetitions of this profile as a function of depth of discharge. Discharge and charge pulses were 5*C* for 18 s and 3.75*C* for 10 s, preceded by 1 h and 32 s rest periods, respectively.

The ac impedance of the fully charged cells was measured by Solartron 1260 frequency response analyzer with Solartron 1286 electrochemical interface and controlled by impedance software Corrware. The amplitude was 5 mV in a frequency range of 0.01–100 kHz.

Table 1
Electrode specification for pouch cell

| | Anode | Cathode |
|---|---|---|
| Active material | MAG-10 (92%) | $LiNi_{0.8}CO_{0.15}Al_{0.05}O_2$ (84%) |
| Binder | PVdF (8%) | PVdF (8%) |
| Conductive additives | None | Carbon black (4%)/SFG-6 (4%) |
| Electrode thickness (μm; not pressed) | 72 | 70 |
| Loading (mg/$cm^2$) | 4.9 | 8.0 |
| Current collector | Cu (18 μm) | Al (30 μm) |

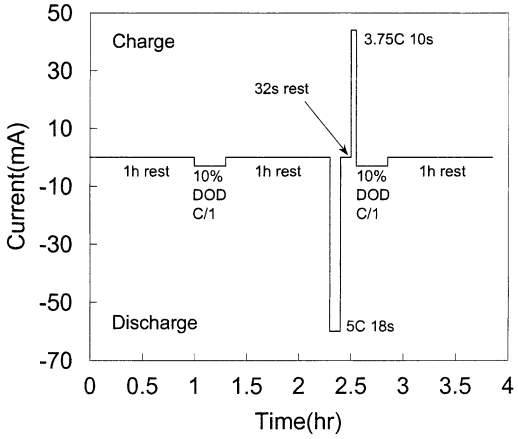


Fig. 1. Hybrid pulse power characterization profile.

## 3. Results and discussion

### 3.1. Cycle performance

The discharge capacity for the three pouch cells in this study, cycled at *C*/2 and room temperature between 0 and 70% DOD (PG70-1000) and 0 and 100% DOD (PG100-480 and PG100-1000) are shown in Fig. 2. The performance of the cells is summarized in Table 2. The capacity losses during *C*/2 cycling at 100% DOD were 30 and 70% at 480 and 1000 cycles, respectively. The cell (PG70-1000) cycled over 70% DOD was able to maintain that capacity for the 1000 cycles. A capacity loss of 14% was measured with a

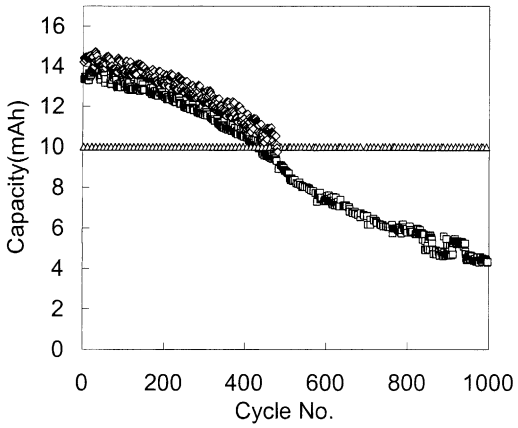


Fig. 2. Cycle performance of pouch cells on different DOD at *C*/2 rate and 25 °C: (◇) PG100-480; (□) PG100-1000; (△) PG70-1000.

Table 2
Cell performance

| Cell | DOD (%) | Cycle number | Capacity fade (%) | | Power fade (%) |
|---|---|---|---|---|---|
| | | | *C*/2 | *C*/25 | |
| PG100-480 | 100 | 480 | 30 | 14 | 70 |
| PG100-1000 | 100 | 1000 | 70 | 40 | NA |
| PG70-1000 | 70 | 1000 | 14 | 11 | 45 |

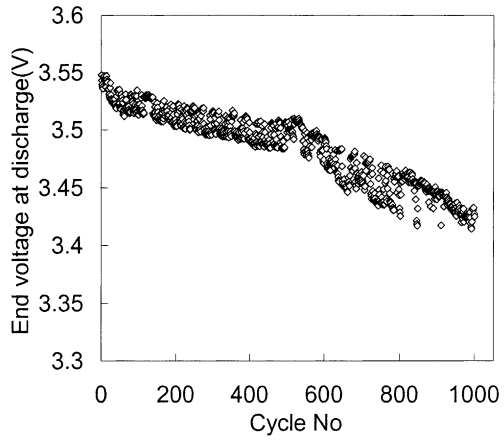


Fig. 3. End voltage of PG70-1000 for discharge during cycling.

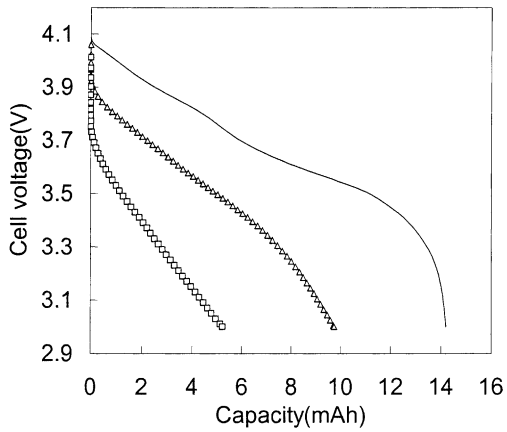


Fig. 4. Voltage profiles of PG100-1000 for discharge on cycling: (—) first cycle; (△) 500th cycle; (□) 1000th cycle.

100% DOD *C*/2 cycle after the 1000 cycles over 70% DOD. The capacity fade for this cell can also be seen in Fig. 3, which shows the end-of-discharge (EOD) voltage during the 70% DOD cycling. This voltage decreased during cycling but never dropped below 3.4 V, even after 1000 cycles. The results in Fig. 2 suggest that a major portion of the capacity fade, during 100% DOD cycling with this chemistry, is occurring during the final insertion of Li into the layered structure, or conversely during the removal of the last Li ions from the carbon anode.

Volume changes with continuous cycling of lithium in and out of intercalation materials can lead to capacity fade through breakdown of the primary particles. The unit cell parameters for $LiNi_{0.8}Co_{0.15}Al_{0.05}O_2$ are reported to be a linear function of SOC between $1 < y < 0.5$ (0–100% SOC) [8]. When 0.5 of lithium is removed from $LiNi_{0.8}Co_{0.15}Al_{0.05}O_2$, the change of unit cell volume can be estimated at only 1.1%. This is a major reason for the good stability of these oxides. The change in volume during cycling would be expected to be even less for the 70% DOD cycled cell, however this difference is most likely not responsible to the differences in performance. XRD analysis of the cathodes from PG70-1000 and PG100-1000 (not shown) show no extra phases and only insignificant changes in the crystallite sizes for the cycled $LiNi_{0.8}Co_{0.15}Al_{0.05}O_2$ compared with the fresh oxide. For the graphite anodes at 100 and 70% DOD, the Li content corresponds to approximately $LiC_{12}$ and $LiC_{18}$, respectively. These compounds are both assigned to the second-stage compound in region (II) [15]. According to Ohzuku et al. [15], there was no change of the repeat distance ($d_n$) for compounds in this stage, only changes in the in-plane lithium ordering. Volume expansion effects cannot explain the differences in capacity fade and the anode should not be a factor in the performance fade rates.

Much literature is devoted to the stability of the layered oxides at high SOC [16]. However, there have been no reports on the stability of $LiNiO_2$, $LiNi_{0.8}Co_{0.2}O_2$ or $LiNi_{0.8}Co_{0.15}Al_{0.05}O_2$ to overdischarge. The materials are reported to be quite stable to atmospheric conductions as-prepared. $LiNiO_2$ can be discharged at around 1.7 V (versus $Li/Li^+$) to a divalent nickel compound, assigned to the redox couple of $Ni^{2+}/Ni^{3+}$ [17]. However, it is unlikely that the trivalent nickel cathodes in our pouch cells convert to divalent compound by overdischarge during constant *C*/2 or even high-rate cycling because the potential for redox couple of $Ni^{2+}/Ni^{3+}$ is too low.

For $Li_{1+y}Mn_{2-y}O_4$, the overpotentials developed during high-rate galvanostatic cycling have been reported to lead to surface gradients in the Li concentration that induce premature transition to the Jahn–Teller distortion and subsequent degradation in this oxide [18]. While no such distortions are expected in $Li_xNi_{0.8}Co_{0.15}Al_{0.05}O_2$, the impedance of this oxide is the highest at $x = 1$ and concentration gradients will be large. A similar argument is possible for the anode with respect to the stability of the SEI layer. However, this electrode is much more conductive. Careful examination of the cathode and anode particles with surface sensitive diagnostics is clearly warranted.

Fig. 4 shows sample voltage profiles for PG100-1000 during *C*/2 cycling. The voltage drop at the beginning of the discharge increased significantly during cycling, suggesting a large rise in the cell impedance. After cycling, the cells were again cycled at very low rate after the *C*/2 cycling. Very low current cycles are also useful to ascertain the amount of cycleable lithium remaining in the limiting electrode (usually the cathode). Fig. 5 shows the voltage profiles for the *C*/25 cycles for PG100-480, PG100-1000 and PG70-1000. These cycles showed capacities of 86 and 60% of the original capacity for PG100-480 and PG100-1000, and 89% of the original capacity remaining for PG70-1000. These data are also summarized in Table 2. The differences in the losses, measured at different rates, are consistent with increases in cell impedance.

Fig. 6 shows the differential capacity plots ($dQ/dV$) for the fresh and cycled cells, calculated from the *C*/25 cycle data. The fresh cell showed three highly reversible peaks

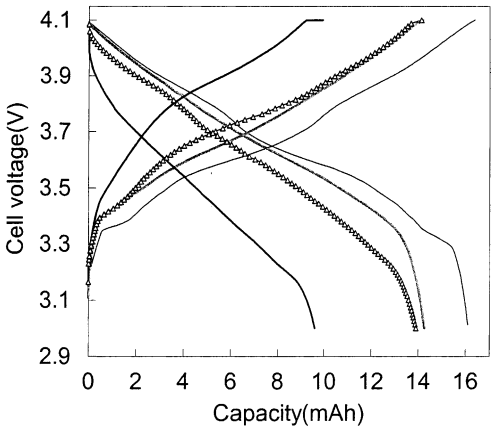


Fig. 5. Cycle profiles of cell at slow rate (*C*/25) before and after cycling: (—) fresh cell; (△) PG100-480; (_) PG100-1000; (_) PG70-1000.

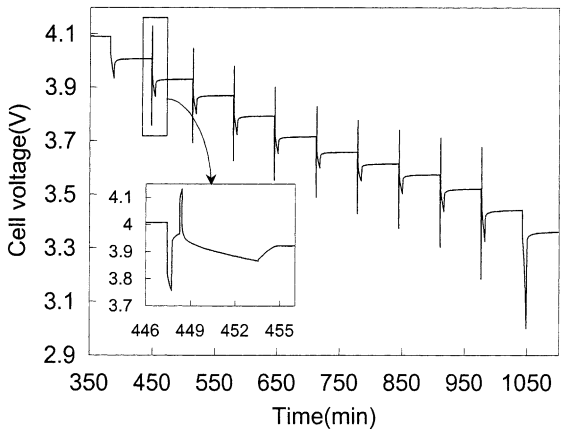


Fig. 7. Voltage profile for hybrid pulse power characterization (HPPC) test.

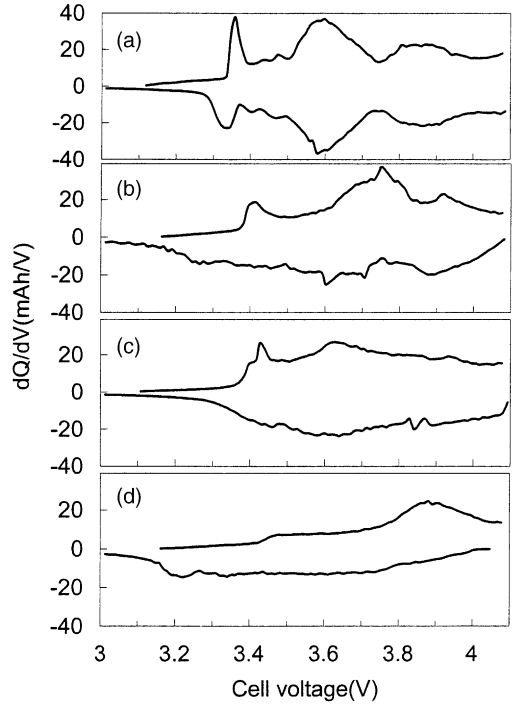


Fig. 6. d*Q*/d*V* plots of cell for slow rate cycle (*C*/25): (a) fresh cell, (b) PG100-480, (c) PG70-1000, (d) PG100-1000.

around 3.33, 3.58 and 3.86 V for charging and discharging, which were assigned to lithium intercalation/deintercalation into/from graphite and doped $LiNiO_2$. However, the cycled cells showed extensive peak shift and/or peak broadening. The d*Q*/d*V* plot for the PG100-1000 showed only one broad peak around 3.9 V for charging. The cell with same components cycled 140 times at 60 °C with 65% loss of capacity showed a very similar shape [8].

### 3.2. Hybrid pulse power characterization

The impedance and power capability of this cell with cycling is important in its own right for a high-power cell design. In addition, changes in the impedance can be directly responsible for capacity fade, as suggested above. Fig. 7 shows the hybrid pulse power characterization test for a fresh pouch cell. The inset shows a blow-up of the pulse sequence, as described in detail above. The 18 s discharge area specific impedance (ASI) and discharge pulse power capability are calculated as in Eqs. (1) and (2):

$$\text{ASI} = \frac{\Delta V}{\Delta I} = \frac{V_{t_0} - V_{t_1}}{I_{t_0} - I_{t_1}} \quad (1)$$

$$\text{discharge pulse power capability} = \frac{V_{\min}(\text{OCV} - V_{\min})}{R_{\text{discharge}}} \quad (2)$$

where $t_0$ is the starting point of discharge pulse, $t_1$ is the end-point of the discharge pulse, OCV is the open circuit voltage and $V_{\min}$ is the lower cut-off voltage. Only the discharge values are considered in this paper. The Regen (charging) resistances are dependent on the concentration gradients built-up during discharge with only a 32 s rest period between the pulses, and are therefore less informative. As cycling progressed, the cells were not able to support the 5*C* discharge current for the full 18 s as far into the discharge. At 480 cycles, the HPPC test could be carried out only until 60% DOD. Figs. 8 and 9 show the variation of ASI and pulse power capability on DOD and cycling. The ASI of PG100-480 increased by a factor of 2.5 compared to the fresh cell and the discharge pulse power capability decreased to 30% of the original power capability. Although PG100-480 showed just 30% of capacity fading for constant cycling in Fig. 2, its power fading was almost 70% because of large increase of cell resistance. In contrast, the PG70-1000 showed similar ASI values to that of PG100 at only the 240th cycle. Limiting the discharge to 70% DOD clearly improves the maintenance of the conductivity as well as the capacity of this cell. Several reports of impedance rise in lithium-ion cells conclude that the bulk of the change is attributable to the cathode. Wu et al. [3] reported the variation of cell impedance in commercial lithium-ion cell with a reference electrode. They observed

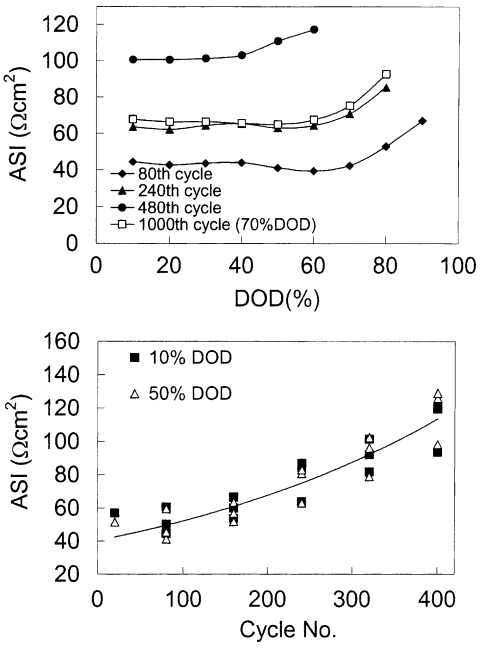


Fig. 8. Area specific impedances of PG100-480 and PG70-1000 on cycling under HPPC test.

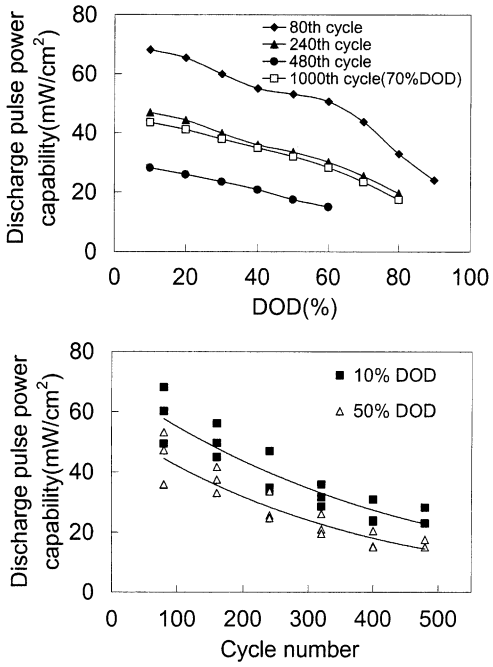


Fig. 9. Discharge pulse power capability of PG100-480 and PG70-1000 on cycling under HPPC test.

that a large increase in the cathode impedance was the main reason for cell impedance increase after a 40% capacity loss.

### 3.3. Electrochemical impedance spectroscopy

The impedance characteristics of these pouch cells were also examined with electrochemical impedance spectroscopy (EIS). Commercial and lab-scale lithium-ion cells with graphite and metal oxide usually show two semicircles of different size at the high (or medium) and low frequency in a Nyquist plot [19–22]. The Nyquist plots of fresh and cycled cells, shown in Fig. 10, exhibit profiles similar to those described by other researchers. The smaller high-frequency semicircle was depressed slightly and did not change much with cycling. However, the size of the larger low-frequency semicircle for the PG100-480 increased significantly while that for the PG70-1000 increased only slightly. These results are consistent with the HPPC measurements.

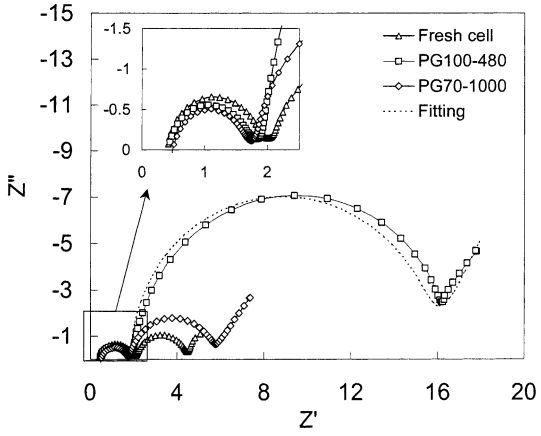


Fig. 10. Nyquist plots of fully charged cell before and after cycling: (△) fresh cell; (□) PG100-480; (◇) PG70-1000; (---) fitting.

The high-frequency intercept of the Nyquist plot with the real axis represents the ohmic resistance of the cell including electronic resistances of electrode, current collectors, leads, and electrolyte resistance [20,21]. Since the electronic resistance of well-made electrodes can usually be neglected, the ohmic resistance comes mainly from the electrolyte. Fig. 11 shows a simple equivalent circuit proposed for the Li-ion cell [20,23]. $CPE_1$ and $CPE_2$ represent constant phase elements, and $R_\Omega$, $R_1$ and $R_2$ are the ohmic resistance and the resistance of first and second semicircles, respectively. $Z_W$ is the Warburg impedance due to the lithium-ion diffusion within the particle. The charge transfer resistances, $R_1$ and $R_2$, result from the interface resistance of both anode/electrolyte and cathode/electrolyte. Researchers have reported the growth of the surface films on the anode and the formation of defect in cathode material, but usually conclude that the cathode contributes more to the increase of overall cell impedance [20,22,24,25]. Nagasubramanian observed that the cathode contributed the most to the second semicircle from three-electrode impedance test [19].

The impedance parameters for the fresh and cycled cells obtained via fitting are listed in Table 3. $R_\Omega$ and $R_1$ are almost constant after cycling but $R_2$ increased in comparison to the fresh cell. As described above, the interface resistance of both anode and cathode contribute to both $R_1$ and $R_2$. The changes for $R_1$ and $R_2$, shown in Table 3, are consistent with the changes in cell impedance shown in Fig. 8.

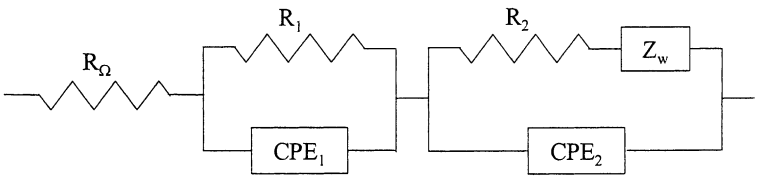


Fig. 11. Equivalent circuit for pouch Li-ion cell.

Table 3
Impedance parameters from fresh and cycled cells

| Cell | Voltage (V) | $R_\Omega$ (Ω) | $R_1$ (Ω) | $R_2$ (Ω) |
|---|---|---|---|---|
| Fresh cell | 4.08 | 0.47 | 1.45 | 2.66 |
| PG100-480 | 3.98 | 0.46 | 1.41 | 13.84 |
| PG100-1000 | 3.95 | 0.46 | 1.89 | 96.89 |
| PG70-1000 | 4.07 | 0.49 | 1.28 | 3.95 |

### 3.4. Electrochemical analysis

After cycling, the cells were disassembled and each electrode was tested against Li metal in a half-cell. Fig. 12 shows the *C*/25 voltage profiles for the cycled anodes taken from the pouch cells in comparison with a fresh anode. All anodes showed about the same capacity of 340 mAh/g, even after 1000 cycles at 100% DOD.

The charge/discharge profiles for fresh and cycled cathodes at *C*/25 are shown in Fig. 13. These cathodes showed different behavior depending on the type of cycling. The *C*/25 capacity losses for the cycled cathodes show the same trends as the *C*/25 cycle data from the full cells, which were shown in Fig. 5. The differences between the *C*/25 loss in the cell and that in the cathode can be tentatively assigned to consumption of Li by side-reactions in the cell. This difference ranged from 0 to 16%. From Figs. 12 and 13, we can conclude that none of the capacity fade can be directly attributed to the anode, except as a consumer of cycleable Li. This process will be discussed further in Part II.

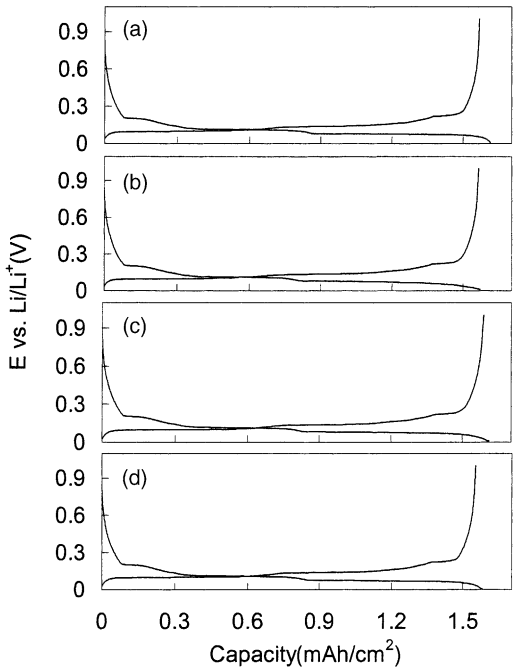


Fig. 12. Voltage profiles of anode against Li metal in half-cell: (a) fresh anode, (b) PG100-480, (c) PG100-100, (d) PG70-1000.

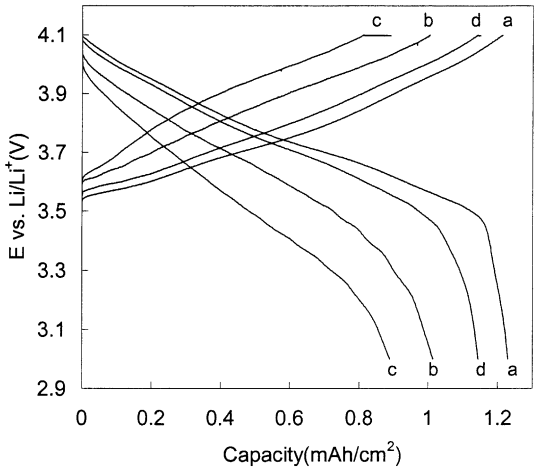


Fig. 13. Voltage profiles of cathodes against Li metal in half-cell: (a) fresh cathode, (b) PG100-480, (c) PG100-1000, (d) PG70-1000.

The real losses of the cycled cathodes, exemplified in Fig. 13, can be attributed either to film formation on the cathode particles or to a breakdown of the cathode structure, either through degradation of the oxide or loss of the conductive carbon [8], all of which will lead to isolation of Li-containing cathode material due to high-impedance pathways to parts of the electrode. We can say that most of the capacity fade in these cells comes from the loss of accessible Li sources in the cathode through high-impedance pathways, not from the loss of Li inventory by continuous side-reaction. Further diagnostics, including TEM, FTIR, and Raman spectroscopies of the cell components after cycling will be reported in Part II and examined carefully to further identify the nature of the high-impedance pathway, either through film formation or particle isolation, and to explain the higher rates of performance degradation during higher DOD cycling.

## 4. Conclusions

The room temperature cycle performance and pulse power capability of lithium-ion cells with graphite and

$LiNi_{0.8}Co_{0.15}Al_{0.05}O_2$ were studied for different DOD cycling. Cycling this cell to 100% DOD, or 3.0 V, leads to significantly faster rates of both capacity fade and impedance rise, compared to cells limited to 70% DOD. The cell cycled 1000 times at 100% DOD was unable to access 40% of the lithium between 3.0 and 4.1 V even at a *C*/25 rate. The cell cycled 1000 times at 70% DOD showed only a 14% loss in high-rate capacity and only a 45% loss of power. The large capacity and power losses in this cell chemistry come mainly from increases in the bulk and/or interfacial impedance of the cathode.

## Acknowledgements

We would like to thank T. Richardson for the XRD analysis of the cycled cathodes. This work was supported by the Assistant Secretary for Energy Efficiency and Renewable Energy, Office of Freedom CAR and Vehicle Technologies of the US Department of Energy under Contract No. DE-AC03-76SF00098.

## References

[1] A.N. Jansen, A.J. Kahaian, K.D. Kepler, P.A. Nelson, K. Amine, D.W. Dees, D.R. Vissers, M.M. Thackeray, J. Power Sources 81–82 (1999) 902.
[2] G. Nagasubramanian, R.G. Jungst, D.H. Doughty, J. Power Sources 83 (1999) 193.
[3] Q. Wu, W. Lu, J. Prakash, J. Power Sources 88 (2000) 237.
[4] Advanced Technology Development, 1999 Annual Progress Report, US DOE, OAAT, March 2000.
[5] PNGV battery test manual, INEEL, DOE/ID-10597, Review 3, 2001.
[6] R.B. Wright, et al., 200th ECS meeting, Abstracts #129–131, San Francisco, September 2001.
[7] X. Zhang, P.N. Ross, R. Kostecki, F. Kong, S. Sloop, J.B. Kerr, K.A. Striebel, E.J. Cairns, F. McLarnon, J. Electrochem. Soc. 148 (2001) A463.
[8] J. Shim, R. Kostecki, T. Richardson, X. Song, K.A. Striebel, J. Power Sources 112 (2002) 222.
[9] K.A. Striebel, J. Shim, LBNL-50500, Berkeley, CA, June 2002.
[10] M. Balasubramanian, X. Sun, X.Q. Yang, J. McBreen, J. Electrochem. Soc. 147 (2000) 2903.
[11] J. Cho, H. Jung, Y. Park, G. Kim, H. Lim, J. Electrochem. Soc. 147 (2000) 15.
[12] K.-K. Lee, K.-B. Kim, J. Electrochem. Soc. 147 (2000) 1709.
[13] J. Cho, B. Park, J. Power Sources 92 (2001) 35.
[14] J. Shim, R. Kostecki, T. Richardson, G. Zhuang, Y. Lee, X. Song, P.N. Ross, E.J. Cairns, K.A. Striebel, in preparation.
[15] T. Ohzuku, Y. Iwakoshi, K. Sawai, J. Electrochem. Soc. 140 (1993) 2490.
[16] S. Madhavi, G.V. Subba Rao, B.V.R. Chowdari, S.F.Y. Li, J. Power Sources 93 (2001) 156.
[17] J. Maruta, H. Yasuda, M. Yamachi, J. Power Sources 90 (2000) 89.
[18] Y. Shao-Horn, S.A. Hackney, A.J. Kahaian, K.D. Kepler, F. Skinner, J.T. Vaughey, M.M. Thackeray, J. Power Sources 81–82 (1998) 496.
[19] G. Nagasubramanian, J. Power Sources 87 (2000) 226.
[20] J. Li, E. Murphy, J. Winnick, P.A. Kohl, J. Power Sources 102 (2001) 294.
[21] C.H. Chen, J. Liu, K. Amine, J. Power Sources 96 (2001) 321.
[22] D. Zhang, B.S. Haran, A. Durairajan, R.E. White, Y. Podrazhansky, B.N. Popov, J. Power Sources 91 (2000) 122.
[23] S. Rodrigues, N. Munichandraiah, A.K. Shukla, J. Solid State Electrochem. 3 (1999) 397.
[24] J. Li, E. Murphy, J. Winnick, P.A. Kohl, Power Sources 102 (2001) 302.
[25] Y. Kida, A. Kinoshita, K. Yanagida, A. Funahashi, T. Nohma, I. Yonezu, Electrochim. Acta 47 (2002) 1691.